# *High-fidelity quantum state evolution in imperfect photonic integrated circuits*

# High-fidelity quantum state evolution in imperfect photonic integrated circuits

Jacob Mower,[1] Nicholas C. Harris,[1] Gregory R. Steinbrecher,[1] Yoav Lahini,[2] and Dirk Englund[1,*]

[1]*Department of Electrical Engineering and Computer Science, Massachusetts Institute of Technology, 77 Massachusetts Avenue, Cambridge, Massachusetts 02139, USA*

[2]*Department of Physics, Massachusetts Institute of Technology, 77 Massachusetts Avenue, Cambridge, Massachusetts 02139, USA*

(Received 9 June 2014; revised manuscript received 6 February 2015; published 22 September 2015)

We propose and analyze the design of a programmable photonic integrated circuit for high-fidelity quantum computation and simulation. We demonstrate that the reconfigurability of our design allows us to overcome two major impediments to quantum optics on a chip: it removes the need for a full fabrication cycle for each experiment and allows for compensation of fabrication errors using numerical optimization techniques. Under a pessimistic fabrication model for the silicon-on-insulator process, we demonstrate a dramatic fidelity improvement for the linear optics controlled-NOT and controlled-PHASE gates and, showing the scalability of this approach, the iterative phase estimation algorithm built from individually optimized gates. We also propose and simulate an experiment that the programmability of our system would enable: a statistically robust study of the evolution of entangled photons in disordered quantum walks. Overall, our results suggest that existing fabrication processes are sufficient to build a quantum photonic processor capable of high-fidelity operation.

DOI: 10.1103/PhysRevA.92.032322 PACS number(s): 42.50.Ex, 42.50.Dv, 42.82.Bq, 42.79.Ta

## I. INTRODUCTION

Photonic integrated circuits (PICs)—waveguide-based systems of optical elements such as beam splitters and phase shifters that are monolithically integrated on a single chip—enable control over the propagation and coupling of optical modes with exceptional phase stability and at the scale of tens to hundreds of waveguides. In particular, PICs fabricated using mature silicon processes have seen rapid development in recent years for optical interconnects and other classical applications [1,2]. Additionally, PICs have been shown to be an appealing platform for quantum optics: PIC-based experiments have demonstrated quantum simulation [3–5], boson sampling [6–8], linear optical quantum gates [9,10], and the simulation of bosonic quantum walks [5,11,12].

One of the main impediments to quantum optics experiments on PICs has been the need to fabricate custom chips for each experiment, an expensive and time consuming process. In addition, many applications require PICs to be tuned between consecutive experiments. While some experiments have shown on-chip reconfigurability [13–15], there has been to date no analysis of a fully reconfigurable PIC that can implement arbitrary circuits. Additionally, PIC-based experiments to date have suffered from reduced fidelity due to variations and imperfections in the fabrication process.

In this work, we propose and analyze the design of a reconfigurable quantum photonic processor (QPP)—achievable with existing, mature silicon processes—that overcomes fabrication imperfections. We demonstrate how to program arbitrary transformations into this system and, using a fabrication model with conservative assumptions on technology, demonstrate a tuning algorithm that overcomes fabrication imperfections and achieves high-fidelity quantum operations. This programmable linear optics circuit would enable the rapid testing of quantum optics algorithms.

In the next section, we introduce the QPP architecture and discuss the origins of imperfections in realistic devices. Section III shows how to implement quantum gates on a QPP, quantifies the detrimental effects of fabrication errors, and then demonstrates a computationally scalable, gate-by-gate procedure that allows us to recover high-fidelity gate operation. As an example of the power of this technique, we analyze a circuit implementing a full quantum algorithm, the iterative phase estimation algorithm (IPEA), and show that gate-by-gate optimization is sufficient for high-fidelity operation of the full circuit. Next, in Sec. V, we propose and simulate a bosonic transport experiment that leverages the reconfigurability of the QPP to investigate 1000 realizations of quantum walks under a range of disorder and decoherence levels and to perform state preparation on a pair of input photons. To close, we discuss methods of extending this architecture with recent advances in integrated quantum devices.

## II. QPP ARCHITECTURE

The proposed QPP architecture consists of a lattice of $2 \times 2$ building blocks [Fig. 1(a)], each of which is a Mach-Zehnder interferometer (MZI) [Fig. 1(d)] [18]. In the spatial mode basis, an ideal MZI applies the $2 \times 2$ unitary given by

$$U_{\mathrm{MZI}}(\theta,\phi) = \frac{1}{2}\begin{pmatrix} e^{i\phi} & 0 \\ 0 & 1 \end{pmatrix}\begin{pmatrix} 1 & i \\ i & 1 \end{pmatrix}\begin{pmatrix} e^{i\theta} & 0 \\ 0 & 1 \end{pmatrix}\begin{pmatrix} 1 & i \\ i & 1 \end{pmatrix},$$

where $\theta$ and $\phi$ correspond to the labels in Fig. 1(d).

In realistic integrated optical devices, photon loss, phase errors, and unbalanced beam splitters can severely impact performance. To simulate the effect of these imperfections, we consider a model for the well developed, CMOS-compatible silicon-on-insulator (SOI) platform, based on deep-UV photolithography [19,20]. As photon loss is a primary concern in quantum optics experiments, we have chosen the lowest-loss elements available in this material system: directional couplers [21] for the beam splitters and thermo-optic phase modulators [17].

*Corresponding author: englund@mit.edu

 

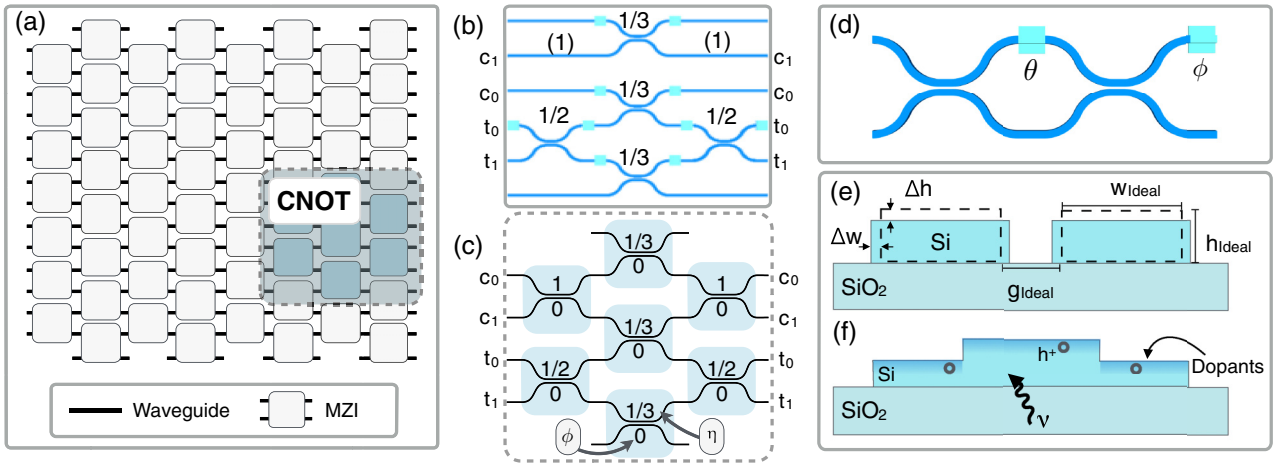


FIG. 1. (Color online) (a) Schematic of the QPP composed of interconnected MZIs. (b) The six-mode CNOT gate proposed in Ref. [16]. (c) The same CNOT protocol implemented on the QPP. The upper number in each box represents the splitting ratio $\eta \equiv \sin^2(\theta)$, where $\theta$ is the internal phase setting, and the lower number represents the output phase offset $\phi$. (d) The MZI unit cell. (e) Cross section of the directional coupler showing the dominant mechanisms for disorder in the splitting ratio, variation in the height of the waveguide $h$, the width $w$, and the waveguide spacing $g$. (f) Cross section of the phase shifter illustrating free carrier absorption, the dominant loss mechanism [17].

Figures 1(e) and 1(f) illustrate the primary causes of nonidealities in these devices: in directional couplers, small variations in the dimensions and spacing of coupled waveguides [Fig. 1(e)] result in varied splitting ratios, while in phase shifters, free carrier absorption in the doped silicon regions [Fig. 1(f)] results in increased propagation loss. Our model accounts for realistic variations by using wafer-scale test results for directional couplers [21] and phase shifters [17]. Wafer-scale test data—as opposed to single-device test data—improves the validity of our model. We model the splitting ratios by a Gaussian distribution with a mean (standard deviation) of 50% (4.3%) [21]. We assume the loss in each thermo-optic modulator is also sampled from a non-negative Gaussian distribution [22] with a mean (standard deviation) of 5.16% (2.84%). While we vary only two phase shifters in each MZI, we include four phase shifters in the design to balance loss [see Fig. 1(d)].

To incorporate these errors into simulations of QPP performance, we need to modify $U_{\mathrm{MZI}}$. First, to account for unbalanced splitting ratios, we make the replacement

$$\frac{1}{\sqrt{2}}\begin{pmatrix}1 & i\\ i & 1\end{pmatrix} \to \begin{pmatrix}\sqrt{t} & i\sqrt{1-t}\\ i\sqrt{1-t} & \sqrt{t}\end{pmatrix}$$

for each directional coupler, where the value of the transitivity $t$ is chosen randomly according to the distribution above.

To incorporate losses—if we wish the analysis to remain unitary—it is necessary to add an additional mode for each lossy component. Then, loss is simply introduced as a beam splitter with reflectivity equal to the loss. However, due to the block structure of the resulting matrix along with the postselected nature of the quantum gates we simulate, we can instead work only with the $2 \times 2$ submatrix corresponding to the waveguide modes. As such, each diagonal element in the $2 \times 2$ phase-shift matrices acquires a factor of $\sqrt{1-\gamma}$, where the values of the $\gamma$'s are distributed according to the loss distribution given above:

$$\begin{pmatrix}e^{i\phi} & 0\\ 0 & 1\end{pmatrix} \to \begin{pmatrix}\sqrt{1-\gamma_1}e^{i\phi} & 0\\ 0 & \sqrt{1-\gamma_2}\end{pmatrix}.$$

## III. HIGH-FIDELITY QUANTUM GATES ON THE QPP

### A. Individual quantum gates

To demonstrate linear optical quantum gates in the QPP architecture, Figs. 1(b) and 1(c) show the postselected linear optical controlled-NOT (CNOT) gate previously implemented in a custom, static PIC [9,23] and the same gate programed into a subset of the (ideal) QPP lattice, respectively. The beam splitting ratio of each MZI in Fig. 1(c) is given by $\eta \equiv \sin^2(\theta)$.

This gate, as well as those discussed later, uses the well known dual-rail encoding, i.e., each qubit is encoded in the photon amplitudes in a pair of modes [24]. The control (target) modes are labeled $c_0$ and $c_1$ ($t_0$ and $t_1$) in the figure. The gate succeeds if and only if a single photon is detected in each pair of modes. Experimental realizations of this gate have demonstrated the promise of PICs, but imperfections in fabrication likely contributed to the reduction in gate fidelities (e.g., to 94% in Ref. [9]). To analyze realistic performance in a QPP system, we simulated 1000 QPPs with splitting ratios and losses given by the aforementioned fabrication model. We then programed the CNOT gate into each QPP.

To evaluate the performance of each gate, each simulation calculates the submatrix corresponding to the input and output computational modes:

$$\frac{1}{2}\begin{pmatrix}e^{i\phi}\sqrt{(1-\gamma_3)t_2} & ie^{i\phi}\sqrt{(1-\gamma_3)(1-t_2)}\\ i\sqrt{(1-\gamma_4)(1-t_2)} & \sqrt{(1-\gamma_4)t_2}\end{pmatrix} \times \begin{pmatrix}e^{i\theta}\sqrt{(1-\gamma_1)t_1} & ie^{i\theta}\sqrt{(1-\gamma_1)(1-t_1)}\\ i\sqrt{(1-\gamma_2)(1-t_1)} & \sqrt{(1-\gamma_2)t_1}\end{pmatrix}.$$

In simulations, the splitting ratios and losses are determined from a Monte Carlo process; these values can be experimentally determined for a real system using methods

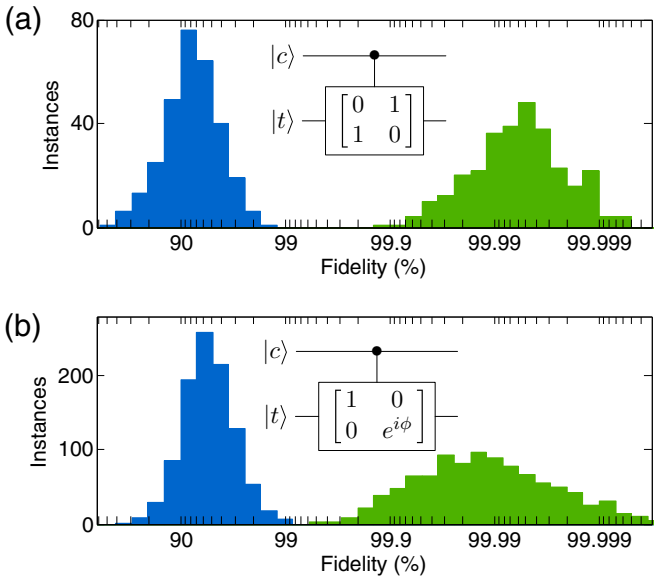


FIG. 2. (Color online) (a) Performance of the CNOT gate for 1000 instances of the QPP. The blue (green) histogram plots the fidelity before (after) optimization of the phase settings. (b) Results pre- and postoptimization for the CPHASE gate over 300 instances of the QPP. For each simulation, the reported fidelity is the minimum over six different choices of $\phi$ (the phase applied by the controlled operation), equally distributed from zero to $2\pi$.

presented in the Supplemental Material [25]. This submatrix can then be used to calculate the $4 \times 4$ transform in the computational (i.e., two-qubit) basis $\{|\mathbf{00}\rangle, |\mathbf{01}\rangle, |\mathbf{10}\rangle, |\mathbf{11}\rangle\}$ [6], after postselection. This is then compared to the ideal transformation with the Hilbert-Schmidt inner product [26] $F(V, V_0) = |\mathrm{tr}(V^\dagger V_0)|$, where $V_0$ is the ideal $4 \times 4$ transform and $V$ is the calculated transform. Normalization (corresponding to postselection) is performed by scaling $V$ and $V_0$ such that $F(V, V) = F(V_0, V_0) = 1$.

The blue histogram in Fig. 2(a) (color online) shows the fidelity of the CNOT gate over the 1000 simulated QPPs, without optimal MZI tuning. These simulations yield a median fidelity of 94.52%, which is similar to experimentally reported values in custom PICs (e.g., [9,27]). We then performed a nonlinear optimization [28–30] of the MZI phase settings [31] to maximize this fidelity for each instance of disorder (see Supplemental Material [25]). The green histogram in Fig. 2(a) (color online) shows the optimized QPP performance; the median fidelity improved dramatically to 99.99%.

We performed the same tuning procedure on the postselected controlled-PHASE (CPHASE) gate of Ref. [32], for which we observe a similar improvement in median fidelity after optimization from 92.22% to 99.99% [see Fig. 2(b)]. These results show that postfabrication optimization enables the reliable implementation of high-fidelity quantum logic gates on QPPs using currently realizable PICs.

### B. Iterative phase estimation algorithm

The possibility of high-fidelity operations makes the QPP architecture attractive for studying larger-scale quantum algorithms. As it is dynamically reconfigurable, it is well suited for iterative algorithms that rapidly update the circuit in response to previous measurements. Here, we examine the performance of one such algorithm, the iterative phase estimation algorithm. The IPEA is an iterative procedure used to solve for the eigenvalues of a Hamiltonian, which has applications in sensing and simulation [3]. The IPEA maps a Hamiltonian $\hat{H}$ to a unitary propagator $\hat{U} \equiv e^{i\hat{H}\tau}$. In this approach, solving the eigenvalue problem $\hat{U}|u\rangle = e^{i2\pi\lambda}|u\rangle$ is equivalent to calculating the energy levels of $\hat{H}$. A binary expansion of $\lambda$ can be calculated by adaptive and iterative bitwise measurements [33,34].

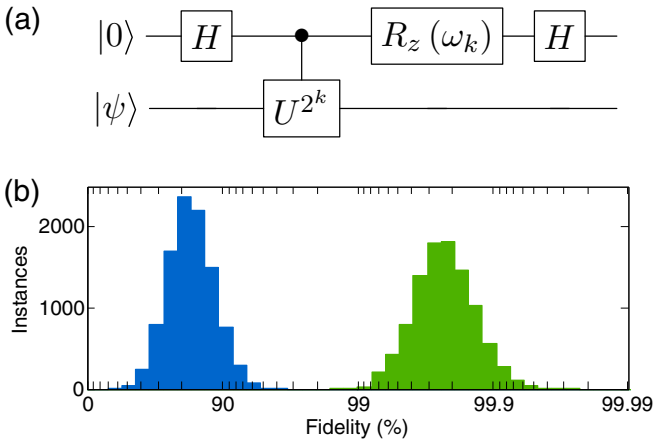


FIG. 3. (Color online) (a) Quantum circuit for the IPEA, as outlined in Ref. [35]. (b) The IPEA fidelity with unoptimized (blue) and optimized (green) performance. By optimizing the circuit to account for fabrication imperfections, the QPP enables very high process fidelities. Again, note the logarithmic scaling to capture both unoptimized and optimized performance on the same axes.

Figure 3(a) shows the quantum circuit for the two qubit IPEA; as demonstrated in [35], this is sufficient to calculate the first four energy levels of an $H_2$ molecule over a range of atomic separations. This is achieved through the use of a basis set in which the Hamiltonian is block-diagonal with at most $2 \times 2$ blocks [36]. To simulate the performance of this system on the QPP, we decompose the controlled unitary of the IPEA into a CPHASE gate with additional single-qubit rotations. We then split the system into three sections that were optimized separately: the input single-qubit rotations, the CPHASE gate, and the output single-qubit rotations. This decomposition into individually optimized gates is useful for computational efficiency.

We find that for 10 000 simulated instances of the QPP, the unoptimized IPEA performed with a median fidelity of 82.63% [Fig. 3(b), blue] (color online). When using our optimized gates, the median fidelity rose to 99.77% [Fig. 3(b), green] (color online). While only two qubits are required for simulating the hydrogen molecule [35], more qubits will be required for simulating larger systems with more complex Hamiltonians. This motivates the development of large-scale PICs such as the QPP.

## IV. QUANTUM RANDOM WALKS

The programmability of the QPP also enables detailed studies of single- [11,37,38] and multiphoton [5,12,39–41]

quantum random walks on a lattice with discrete, nearest-neighbor coupling. These discrete-time quantum random walks (DTQRWs) are attractive for their application to the problems of quantum simulation [42], database search [43], and boson sampling [6].

In the discrete-time QRW, a particle with an internal binary degree of freedom (a "coin") is placed on the lattice. At each step of the walk, two operations occur: the internal state of the coin is prepared and the particle is shifted left or right (as indicated in Fig. 4) according to the state of the coin ("left" and/or "right"). We use a spatial encoding for both the position and the coin state of a quantum walker: position is defined at an MZI, while the coin state is defined by occupation between the two output waveguides of the MZI. The coin toss operation is controlled by the MZI splitting ratio and output phase. The MZI lattice implements a shift operation where photons in the left (right) state propagate left (right) to the next layer of the QPP.

We studied the propagation of two indistinguishable photons on a QRW in the QPP. The path-entangled initial state is $|\psi\rangle_i = (|20\rangle_{\mathrm{LR}} + |02\rangle_{\mathrm{LR}})/\sqrt{2}$, where L and R are the two outputs of the first MZI of the QRW, $\mathrm{MZI}_1$. This state is prepared in the QPP by first launching indistinguishable photons into the two waveguides of the first MZI set to $(\eta,\phi) = (0.5,\pi/2)$, producing the desired state $|\psi\rangle_i$. The next layer of MZIs is set to $(\eta,\phi) = (1,0)$ and $(1,0)$ in order to route the state to the first layer of the random walk. The state is then evolved in the following 15 MZI layers of the QPP, where all internal phases $\theta$ are set to $\pi/2$. In these simulations, disorder is introduced by sampling the MZI output phases ($\phi$) randomly from a uniform distribution on the interval $[0,\Phi_{\mathrm{max}}]$.

We first consider a lattice without disorder, i.e., $\Phi_{\mathrm{max}} = 0$. Simulation results for a realistic QPP are plotted in Figs. 4(a.i)–4(a.iii). Figure 4(a.i) shows the two-photon correlation function, 4(a.ii) plots the particle density at the output, and 4(a.iii) shows the particle density at every layer of the QPP. The two-photon correlation function [Fig. 4(a.i)] displays stronger correlations for neighboring waveguides ("bunching") and particle density peaks at the edges of the array [Figs. 4(a.ii) and 4(a.iii)]. This bunching phenomenon is analogous to Hong-Ou-Mandel interference observed for two input and two output modes [44]. An analogous effect is seen in continuous-time QRWs for two indistinguishable photons launched in neighboring waveguides [5,39].

The impact of disorder on path entanglement and the transport of multiphoton states is not presently well understood, and remains an active area of research. A single realization of disorder offers little information as it can contain extreme arrangements not representative of the majority of lattices with the same level of disorder. This can be seen by comparing a single realization of disorder [Figs. 4(b.i)–4(b.iii)] to 1000

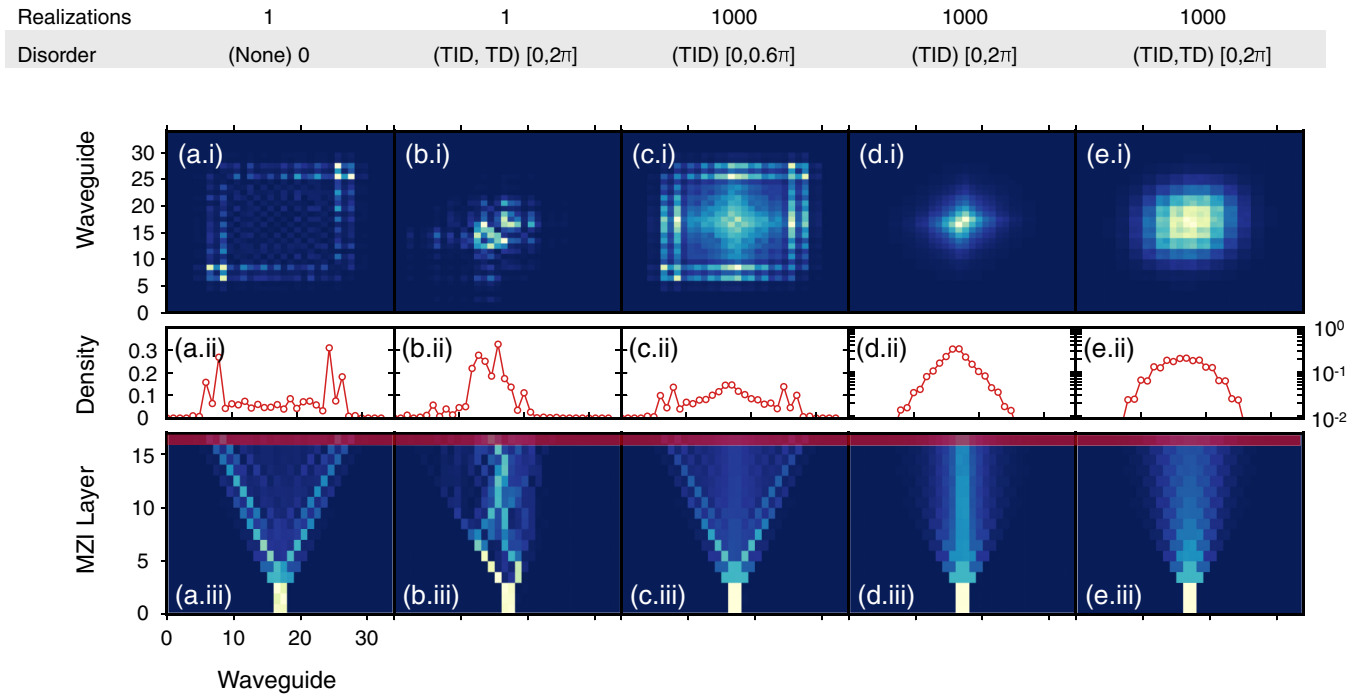


FIG. 4. (Color online) Simulation of the DTQRW in the QPP postselected on detecting two photons for various levels of time-dependent (TD) and time-independent (TID) disorder. (a.i)–(e.i) Correlation functions for output waveguide positions in the QPP lattice. (a.ii)–(e.ii) Particle density distributions as a function of waveguide position [same as the last layer of (a.iii)–(e.iii), marked in red]. (d.ii) and (e.ii) have logarithmic scales. (a.iii)–(e.iii) Dynamics of QRW where the $x$ axis and $y$ axis represent the waveguide output position and MZI layer, respectively. (a.i)–(a.iii) Propagation of input state $(|20\rangle_{\mathrm{LR}} + |02\rangle_{\mathrm{LR}})/\sqrt{2}$ revealing bunching effect seen for continuous-time QRWs. (b.i)–(b.iii) A single realization of TID and TD disorder in the QPP resulting in highly irregular propagation. (c.i)–(c.iii) Average of 1000 realizations of weak TID disorder showing the coexistence of bunching and localization. (d.i)–(d.iii) Average of 1000 realizations of TID disorder showing an exponential density distribution—the hallmark of Anderson localization. (e.i)–(e.iii) Average of 1000 realizations of TID and TD disorder, showing delocalization and a Gaussian distribution.

realizations of disorder [Figs. 4(e.i)–4(e.iii)], for $\Phi_{max} = 2\pi$ in both cases. To build robust statistics, multiple instances of a given level of disorder are required. Until now, this could have been accomplished by fabricating numerous samples or by postprocessing PICs [11,12,38,41]. This approach is difficult to extend to hundreds or thousands of instances. While fast switches could be used to modulate photons passing through a looped QRW [45], there are significant losses associated with this setup that hinder its application to large-scale experiments.

However, a single QPP could generate many instances of disorder. Time-dependent (independent) disorder can be realized with random phase settings along (orthogonal to) the direction of propagation. Applying weak time-independent disorder ($\Phi_{max} = 0.6\pi$) to the lattice results in two-photon correlation and density functions that exhibit both bunched and localized characteristics [Figs. 4(c.i)–4(c.iii)]. This effect was predicted for continuous-time QRWs [40].

Strong, time-independent disorder in the QPP lattice ($\Phi_{max} = 2\pi$) reveals the characteristic exponential distributions of Anderson localization [Figs. 4(d.i)–4(d.iii)]. The incorporation of time-dependent disorder results in the two-photon correlation function and particle density distribution transitioning from exponential localization to Gaussian delocalization [Figs. 4(e.i)–4(e.iii)]—indicative of a crossover to diffusion [46,47]. Although fabrication defects were included in the simulations, we find that the two-photon correlations and densities were largely unaffected (see Supplemental Material [25]).

## V. DISCUSSION

We have shown that a QPP, fabricated in current silicon photonics processes, could enable high-fidelity quantum gates and quantum simulation. We focused on postselected gates to compare this system to preceding PIC-based experiments. Looking forward, one goal of linear optical quantum computing (LOQC) systems is to achieve the error threshold necessary for fault-tolerant quantum computation [24]. For postselected LOQC, this threshold can be as high as 1% [48], but with limitations on overhead (e.g., $<10^4$ physical CNOT gates per qubit and gate), the error rate must be much lower [48]. LOQC requires postselected gates that are heralded by ancilla photons and involve more beam splitters than the gates considered in Sec. III [24,49]. The QPP proposed here offers a path toward achieving the high-fidelity gate operations on-chip that are necessary for LOQC.

Proposed universal quantum computers based on LOQC will also require efficient single-photon sources, single-photon detectors, and feed-forward operations. There has been rapid progress integrating these elements into the silicon photonics platform; recent examples include entangled-photon sources based on four-wave mixing [50,51] and waveguide-integrated superconducting single-photon detectors [52,53]. The potential for multiplexing the emission of spontaneous single-photon sources [54,545 could enable high-efficiency state preparation for quantum computation; low-latency superconducting logic [56] could enable the feed-forward required for scalable LOQC; and low photon-number nonlinear elements could enable photon-photon interaction and deterministic quantum logic [57,58].

The high-dimensional transformations possible on the QPP could also enable a number of applications in classical optics, including multi-input multioutput, transparent, nonblocking switches [59,60], signal routers, high-dimensional beam splitters, and large phased arrays [61], e.g., for LIDAR applications.

## VI. CONCLUSION

We presented a detailed analysis of the feasibility of a reconfigurable quantum photonic processor that enables high-fidelity linear optical transformations and could accelerate prototyping of quantum algorithms in integrated quantum photonics. As demonstrated by our simulation of quantum walks, reconfigurability also enables a single device to perform statistically robust studies of the propagation of photons through complex optical networks. The predicted high fidelity of quantum operations under realistic fabrication defects suggests that a QPP reaching high postselected gate fidelities is within experimental reach.

*Note added.* Recently, J. Carolan *et al.* [62] have reported experiments on a system similar to the one proposed here, and N.C. Harris *et al.* [63] recently reported the experimental demonstration of the architecture proposed here.

## ACKNOWLEDGMENTS

We would like to acknowledge funding from the AFOSR MURI program under Grant No. (FA9550-14-1-0052). J.M. acknowledges support from the iQuISE fellowship and the Claude E. Shannon Research Assistantship. N.C.H. acknowledges that this material is based upon work supported by the National Science Foundation Graduate Research Fellowship under Grant No. 1122374. G.R.S. was supported by the Department of Defense (DoD) through the National Defense Science & Engineering Graduate Fellowship (NDSEG) Program. D.E. acknowledges support from the Sloan Research Fellowship in Physics. Y.L. acknowledges support from the Pappalardo Fellowship in Physics.

J.M., N.C.H., and G.R.S. contributed equally to this work.

[1] W. Green, S. Assefa, A. Rylyakov, C. Schow, F. Horst, and Y. Vlasov, SEMICON, Chiba, Japan, 2010 (unpublished).

[2] D. Miller, IEEE J. Sel. Top. Quantum Electron. **6**, 1312 (2000).

[3] A. Aspuru-Guzik and P. Walther, Nat. Phys. **8**, 285 (2012).

[4] A. Crespi, R. Osellame, R. Ramponi, D. J. Brod, E. F. Galvao, N. Spagnolo, C. Vitelli, E. Maiorino, P. Mataloni, and F. Sciarrino, Nat. Photon. **7**, 545 (2013).

[5] A. Peruzzo, M. Lobino, J. C. F. Matthews, N. Matsuda, A. Politi, K. Poulios, X.-Q. Zhou, Y. Lahini, N. Ismail, K. Wörhoff *et al.*, Science **329**, 1500 (2010).

[6] S. Aaronson and A. Arkhipov, in *Proceedings of the 43rd Annual ACM Symposium on Theory of Computing* (ACM, New York, 2011), pp. 333–342.

[7] M. A. Broome, A. Fedrizzi, S. Rahimi-Keshari, J. Dove, S. Aaronson, T. C. Ralph, and A. G. White, Science **339**, 794 (2012).

[8] J. B. Spring, B. J. Metcalf, P. C. Humphreys, W. S. Kolthammer, X.-M. Jin, M. Barbieri, A. Datta, N. Thomas-Peter, N. K. Langford, D. Kundys *et al.*, Science **339**, 798 (2012).

[9] A. Politi, M. J. Cryan, J. G. Rarity, S. Yu, and J. L. O'Brien, Science **320**, 646 (2008).

[10] E. Martin-Lopez, A. Laing, T. Lawson, R. Alvarez, X.-Q. Zhou, and J. L. O'Brien, Nat. Photon. **6**, 773 (2012).

[11] Y. Lahini, A. Avidan, F. Pozzi, M. Sorel, R. Morandotti, D. N. Christodoulides, and Y. Silberberg, Phys. Rev. Lett. **100**, 013906 (2008).

[12] A. Crespi, R. Osellame, R. Ramponi, V. Giovannetti, R. Fazio, L. Sansoni, F. D. Nicola, F. Sciarrino, and P. Mataloni, Nat. Photon. **7**, 322 (2013).

[13] J. C. F. Matthews, A. Politi, A. Stefanov, and J. L. O'Brien, Nat. Photon. **3**, 346 (2009).

[14] A. Peruzzo, J. McClean, P. Shadbolt, M.-H. Yung, X.-Q. Zhou, P. J. Love, A. Aspuru-Guzik, and J. L. O'Brien, Nat. Commun. **5**, 4213 (2014).

[15] P. J. Shadbolt, M. R. Verde, A. Peruzzo, A. Politi, A. Laing, M. Lobino, J. C. F. Matthews, M. G. Thompson, and J. L. O'Brien, Nat. Photon. **6**, 45 (2012).

[16] T. C. Ralph, N. K. Langford, T. B. Bell, and A. G. White, Phys. Rev. A **65**, 062324 (2002).

[17] N. C. Harris, Y. Ma, J. Mower, T. Baehr-Jones, D. Englund, M. Hochberg, and C. Galland, Opt. Express **22**, 10487 (2014).

[18] M. Reck, A. Zeilinger, H. J. Bernstein, and P. Bertani, Phys. Rev. Lett. **73**, 58 (1994).

[19] T. Baehr-Jones, R. Ding, A. Ayazi, T. Pinguet, M. Streshinsky, N. Harris, J. Li, L. He, M. Gould, Y. Zhang *et al.*, arXiv:1203.0767.

[20] M. Hochberg, N. C. Harris, R. Ding, Y. Zhang, A. Novack, Z. Xuan, and T. Baehr-Jones, Solid-State Circ Mag., IEEE **5**, 48 (2013).

[21] J. C. Mikkelsen, W. D. Sacher, and J. K. Poon, Opt. Express **22**, 3145 (2014).

[22] The continuum limit of a Poisson distribution of scattering events with large mean.

[23] J. L. O'Brien, G. J. Pryde, A. G. White, T. C. Ralph, and D. Branning, Nature (London) **426**, 264 (2003).

[24] E. Knill, R. Laflamme, and G. J. Milburn, Nature (London) **409**, 46 (2001).

[25] See Supplemental Material at http://link.aps.org/supplemental/10.1103/PhysRevA.92.032322 for (1) details of the two-particle, discrete-time quantum random walk simulations; (2) details of the nonlinear optimizations; and (3) proposed methods for the experimental characterization of a fabricated QPP.

[26] M. A. Nielsen and I. L. Chuang, *Quantum Computation and Quantum Information*, 2nd ed. (Cambridge University Press, Cambridge, UK, 2011).

[27] M. Thompson, A. Politi, J. Matthews, and J. O'Brien, IET Circ., Dev. Syst. **5**, 94 (2011).

[28] A. H. G. R. Kan and G. T. Timmer, Math. Program. **39**, 27 (1987).

[29] S. Kucherenko and Y. Sytsko, Comput. Opt. Appl. **30**, 297 (2005).

[30] G. R. Steinbrecher, Y. Lahini, and D. R. Englund (unpublished).

[31] Neither the optimized nor unoptimized CNOT gate programed into the QPP directly implemented the decomposition of the corresponding single-photon unitary transformation proposed in Ref. [12].

[32] K. Kieling, J. L. O'Brien, and J. Eisert, New J. Phys. **12**, 013003 (2010).

[33] A. Aspuru-Guzik, A. D. Dutoi, P. J. Love, and M. Head-Gordon, Science **309**, 1704 (2005).

[34] J. D. Whitfield, J. Biamonte, and A. Aspuru-Guzik, Mol. Phys. **109**, 735 (2011).

[35] B. P. Lanyon, J. D. Whitfield, G. G. Gillett, M. E. Goggin, M. P. Almeida, I. Kassal, J. D. Biamonte, M. Mohseni, B. J. Powell, M. Barbieri *et al.*, Nat. Chem. **2**, 106 (2010).

[36] W. J. Hehre, R. F. Stewart, and J. A. Pople, J. Chem. Phys. **51**, 2657 (1969).

[37] P. W. Anderson, Phys. Rev. **109**, 1492 (1958).

[38] T. Schwartz, G. Bartal, S. Fishman, and M. Segev, Nature (London) **446**, 52 (2007).

[39] Y. Bromberg, Y. Lahini, R. Morandotti, and Y. Silberberg, Phys. Rev. Lett. **102**, 253904 (2009).

[40] Y. Lahini, Y. Bromberg, D. N. Christodoulides, and Y. Silberberg, Phys. Rev. Lett. **105**, 163905 (2010).

[41] G. Di Giuseppe, L. Martin, A. Perez-Leija, R. Keil, F. Dreisow, S. Nolte, A. Szameit, A. F. Abouraddy, D. N. Christodoulides, and B. E. A. Saleh, Phys. Rev. Lett. **110**, 150503 (2013).

[42] M. Mohseni, P. Rebentrost, S. Lloyd, and A. A. Guzik, J. Chem. Phys. **129**, 174106 (2008).

[43] A. M. Childs and J. Goldstone, Phys. Rev. A **70**, 042312 (2004).

[44] C. K. Hong, Z. Y. Ou, and L. Mandel, Phys. Rev. Lett. **59**, 2044 (1987).

[45] A. Schreiber, K. N. Cassemiro, V. Potoček, A. Gábris, I. Jex, and C. Silberhorn, Phys. Rev. Lett. **106**, 180403 (2011).

[46] A. Amir, Y. Lahini, and H. B. Perets, Phys. Rev. E **79**, 050105 (2009).

[47] L. Levi, Y. Krivolapov, S. Fishman, and M. Segev, Nat. Phys. **8**, 912 (2012).

[48] E. Knill, Nature (London) **434**, 39 (2005).

[49] R. Okamoto, J. L. O'Brien, H. F. Hofmann, and S. Takeuchi, Proc. Natl. Acad. Sci. USA **108**, 10067 (2011).

[50] J. Chen, Z. H. Levine, J. Fan, and A. L. Migdall, Opt. Express **19**, 1470 (2011).

[51] N. C. Harris, D. Grassani, A. Simbula, M. Pant, M. Galli, T. Baehr-Jones, M. Hochberg, D. Englund, D. Bajoni, and C. Galland, Phys. Rev. X **4**, 041047 (2014).

[52] F. Najafi, J. Mower, N. C. Harris, F. Bellei, A. Dane, C. Lee, X. Hu, P. Kharel, F. Marsili, S. Assefa *et al.*, Nat. Commun. **6**, 5873 (2015).

[53] W. Pernice, C. Schuck, O. Minaeva, M. Li, G. N. Goltsman, A. V. Sergienko, and H. X. Tang, Nat. Commun. **3**, 1325 (2012).

[54] A. L. Migdall, D. Branning, and S. Castelletto, Phys. Rev. A **66**, 053805 (2002).

[55] J. Mower and D. Englund, Phys. Rev. A **84**, 052326 (2011).

[56] A. N. McCaughan and K. K. Berggren, Nano Lett. **14**, 5748 (2014).

[57] M. Gullans, D. E. Chang, F. H. L. Koppens, F. J. García de Abajo, and M. D. Lukin, Phys. Rev. Lett. **111**, 247401 (2013).

[58] I. Fushman, D. Englund, A. Faraon, N. Stoltz, P. Petroff, and J. Vuckovic, Science **320**, 769 (2008).

[59] M. Yang, W. M. J. Green, S. Assefa, J. V. Campenhout, B. G. Lee, C. V. Jahnes, F. E. Doany, C. L. Schow, J. A. Kash, and Y. A. Vlasov, Opt. Express **19**, 47 (2010).

[60] Q. Chen, F. Zhang, R. Ji, L. Zhang, and L. Yang, Opt. Express **22**, 12614 (2014).

[61] J. Sun, E. Timurdogan, A. Yaacobi, E. S. Hosseini, and M. R. Watts, Nature (London) **493**, 195 (2013).

[62] J. Carolan, C. Harrold, C. Sparrow, E. Martín-López, N. J. Russell, J. W. Silverstone, P. J. Shadbolt, N. Matsuda, M. Oguma, M. Itoh, G. D. Marshall, M. G. Thompson, J. C. F. Matthews, T. Hashimoto, J. L. O'Brien, and A. Laing, Science **349**, 711 (2015).

[63] N. C. Harris, G. R. Steinbrecher, J. Mower, Y. Lahini, M. Prabhu, T. Baehr-Jones, M. Hochberg, S. Lloyd, and D. Englund, arXiv:1507.03406 [quant-ph].